nature physics

LETTERS

https://doi.org/10.1038/s41567-020-0841-9

Check for updates

Topological turbulence in the membrane of a living cell

Tzer Han Tan[1,3], Jinghui Liu[1,3], Pearson W. Miller[1,3], Melis Tekant[1], Jörn Dunkel[2]✉ and Nikta Fakhri[1]✉

Topological defects determine the structure and function of physical and biological matter over a wide range of scales, from the turbulent vortices in planetary atmospheres, oceans or quantum fluids to bioelectrical signalling in the heart[1–3] and brain[4], and cell death[5]. Many advances have been made in understanding and controlling the defect dynamics in active[6–9] and passive[9,10] non-equilibrium fluids. Yet, it remains unknown whether the statistical laws that govern the dynamics of defects in classical[11] or quantum fluids[12–14] extend to the active matter[7,15,16] and information flows[17,18] in living systems. Here, we show that a defect-mediated turbulence underlies the complex wave propagation patterns of Rho-GTP signalling protein on the membrane of starfish egg cells, a process relevant to cytoskeletal remodelling and cell proliferation[19,20]. Our experiments reveal that the phase velocity field extracted from Rho-GTP concentration waves exhibits vortical defect motions and annihilation dynamics reminiscent of those seen in quantum systems[12,13], bacterial turbulence[15] and active nematics[7]. Several key statistics and scaling laws of the defect dynamics can be captured by a minimal Helmholtz–Onsager point vortex model[21] as well as a generic complex Ginzburg–Landau[22] continuum theory, suggesting a close correspondence between the biochemical signal propagation on the surface of a living cell and a widely studied class of two-dimensional turbulence[23] and wave[22] phenomena.

Topological defects are persistent discontinuities in the order-parameter fields[22,24] of continuum physical systems. Such defects critically determine the structure of fluids[25,26], the rigidity of solids[24,27] and the dynamics of biological matter[5,6,28]. The analysis and classification of topological defects offers a unified framework for comparing essential structural properties across a wide range of equilibrium and non-equilibrium systems, from point vortices[11,21] and vortex lines in water[10,25,26], plasmas[29] and quantum gases[12,13,30,31] to dislocations in crystals and disclinations in liquid crystals[24]. Recent experimental advances in the imaging of cells and tissues have revealed the importance of topological defects for a range of biological processes such as collective multicellular migration[32], cell extrusion and death[5], opening new pathways towards the engineering of biomimetic materials such as active liquid crystals[28].

A particularly interesting class of dynamical defects that has profound implications for morphogenesis and complex biological functions underlies the formation of spiral wave patterns in reaction–diffusion systems[33,34]. Extensively studied in Belousov–Zhabotinsky[35] and surface reactions[36], spiral waves rotate around phase field defects and can exhibit complex state transition dynamics[37], chimaera behaviour[38] and defect-mediated turbulence[22,39]. Topologically similar biochemical patterns have been shown to play important roles in many multicellular signalling and self-organization processes in lower[40] and higher[1] forms of life. In the heart[1–3] or brain[4], for example, the presence of topological defects in the phase fields of bioelectrical signalling waves has been associated with arrhythmia and sleep-like states, respectively. However, despite such substantial progress in the understanding of topological defects and their functional implications, it is not yet clear whether statistical laws that govern such topological structures in classical[11] and quantum systems[14,41,42] extend to living matter[43].

To investigate this question in vivo, we examined the dynamics of self-sustained biochemical wave patterns on the oocyte membranes of the starfish *Patiria miniata*. The starfish oocyte membrane is a two-dimensional (2D) excitable medium[20], capable of sustaining self-organized waves of a membrane-bound signalling protein, Rho-GTP (GTP, guanosine triphosphate), for tens of minutes (Fig. 1a). We imaged Rho-GTP using the enhanced green fluorescent protein/rhotekin GTPase binding domain (GFP-rGBD) biosensor (11 videos from 7 oocytes) and observed a variety of non-equilibrium steady states, four of which are shown in Fig. 1b (fluorescence intensity is proportional to the concentration of the Rho-GTP on the membrane; Supplementary Videos 1–4). Each of these steady states presents a different spatiotemporal wave pattern, with typical wavelengths ranging from 15 to 30 μm (Fig. 1c). As the Rho-GTP waves pass through a point on the 2D membrane, they produce an oscillatory fluorescent intensity signal that is recorded on the microscope camera pixel (resolution of 0.6 μm) monitoring that membrane position (Extended Data Fig. 1a). The pixel oscillation periods for different waves ranged from 50 s to 120 s (Fig. 1d). From the time series of pixel intensity oscillations one can extract the relative phases across the membrane using a time-delay embedding algorithm[1] (Extended Data Fig. 1 and Methods). This analysis yields the phase field $\phi(\mathbf{x}, t)$ associated with the Rho-GTP concentration field.

The phase field $\phi(\mathbf{x}, t)$ harbours a dense population of topological defects (Fig. 1e). Such phase defects are singular points where neighbouring phase values jump discontinuously. The defects can be characterized by analysing the local wavevector field, defined as the gradient of the phase field $\mathbf{V}_\phi(\mathbf{x}, t) = \nabla\phi(\mathbf{x}, t)$ (Fig. 2a(iii)). The topological charge of a defect is given by the integer-valued winding number, $\Gamma = \frac{1}{2\pi}\oint_C \nabla\phi \cdot \mathrm{d}\mathbf{s}$, where C is a closed contour around the defect that encloses no other defects. The phase field defects observed in our experimental data generally have winding numbers of +1 or −1, corresponding to counterclockwise or clockwise rotating local phase field dynamics (Fig. 1f and Supplementary Video 5). We find that, within the field of view (~300 μm × 300 μm) and

[1]Department of Physics, Massachusetts Institute of Technology, Cambridge, MA, USA. [2]Department of Mathematics, Massachusetts Institute of Technology, Cambridge, MA, USA. [3]These authors contributed equally: Tzer Han Tan, Jinghui Liu, Pearson W. Miller. ✉e-mail: dunkel@mit.edu; fakhri@mit.edu

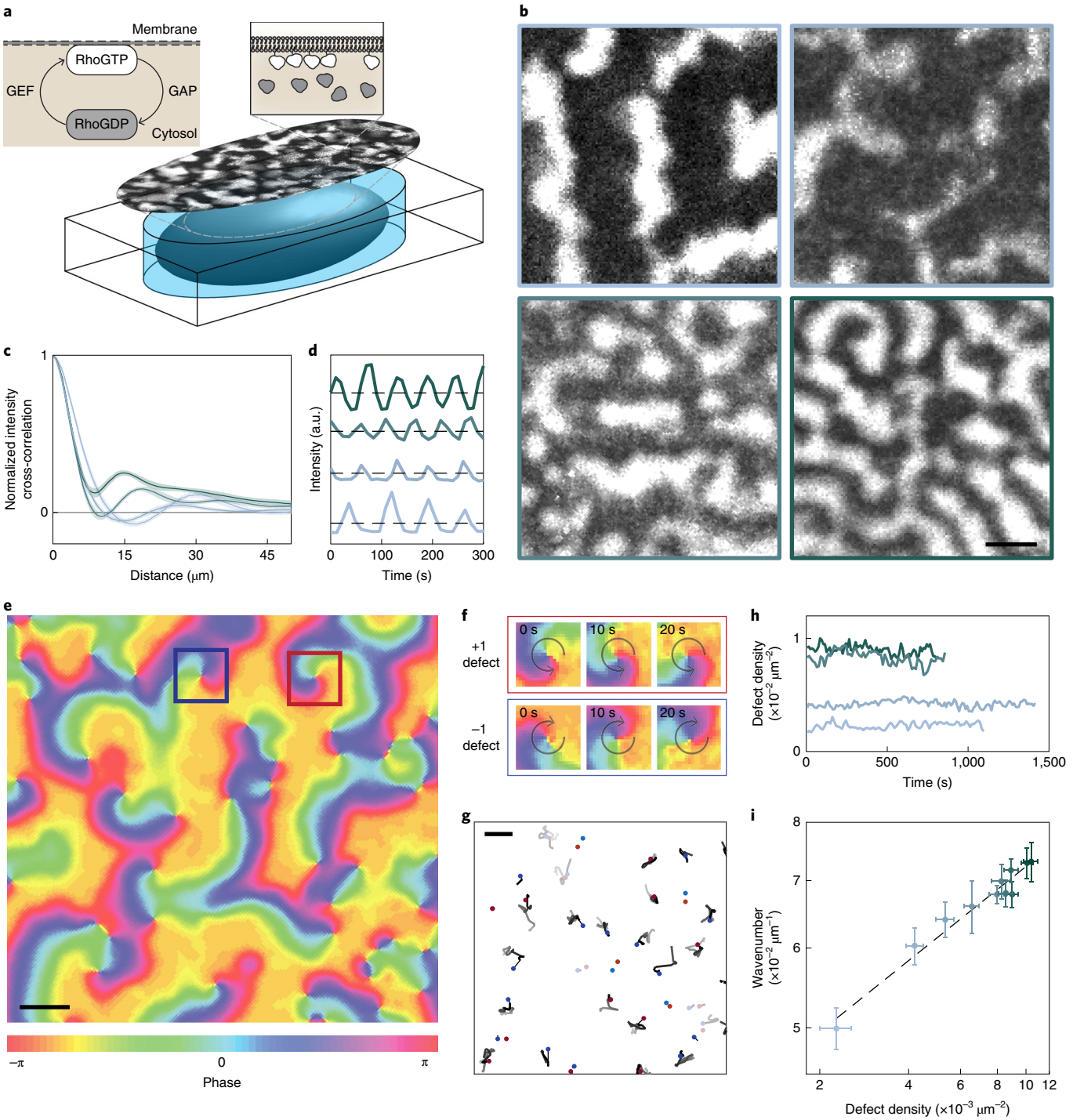

Fig. 1 | Topological defects populate the phase field of Rho-GTP waves on the starfish oocyte membrane. a, Membrane Rho-GTP waves are visualized with GFP-rGBD reporter in live starfish oocytes. Oocytes are confined in elliptical polydimethylsiloxane (PDMS) chambers to minimize sample drift during time-lapse imaging. Inset: cycling of Rho protein between the GTP-bound (active) state on the membrane and guanosine diphosphate (GDP)-bound (inactive) state in the cytosol. GEF is the guanine nucleotide exchange factor and GAP is the GTPase-activating protein. **b**, Representative snapshots of Rho-GTP waves from four oocytes at different steady states. Scale bar, 15 μm. **c**, Normalized intensity cross-correlation plotted as a function of distance for the four states shown in **b**. Error bars represent s.e. throughout time. **d**, Representative time series of fluorescence intensity at the single pixel level for the four states shown in **b** (colours of lines match the outlines of the images in **b**). **e**, A representative phase field reconstructed from pixel oscillations harbours a dense population of topological defects. The defects in the red and blue squares have winding numbers +1 and −1, respectively. Scale bar, 15 μm. **f**, Time-lapse snapshots of the phase field in the vicinity of a topological defect every 10 s. The +1 and −1 defects exhibit counterclockwise and clockwise rotating dynamics, respectively. **g**, Trajectories of defects undergoing creation (black) and annihilation (grey) events. Both types of events always involve pairs of oppositely charged defects (red, +1; blue, −1). Scale bar, 10 μm. **h**, The defect density fluctuates about a constant value at steady state. **i**, Characteristic wave numbers are positively correlated with defect density for all 11 states. Error bars represent s.d. Dashed line is the line of the best fit.

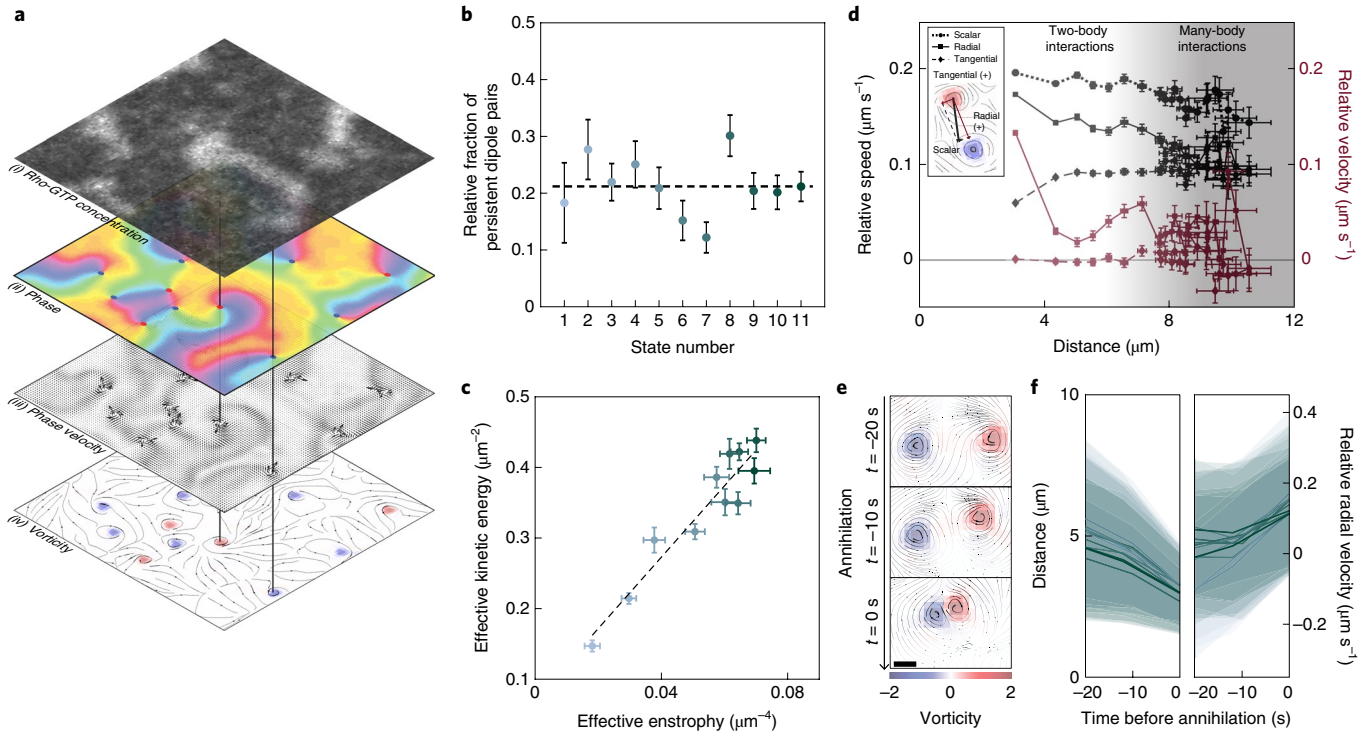

Fig. 2 | Vortex dynamics in the phase velocity field. a, Different dynamical fields underlie self-sustained Rho-GTP waves in starfish oocyte membrane (i). From the constructed phase field $\phi(\mathbf{x}, t)$ (ii), the phase velocity field, $\mathbf{V}_\phi(\mathbf{x}, t) = \nabla\phi(\mathbf{x}, t)$ (iii) can be computed. Vortex dynamics in the phase velocity field is visualized using a vorticity contour line (iv). **b**, Relative fraction of persistent dipole pairs for all 11 states, showing signatures reminiscent of a low-energy BKT phase. Error bars represent s.d. throughout time. The dashed line represents the mean fraction averaged over the 11 states. **c**, Mean effective kinetic energy, $\bar{E}$, for each of the 11 states shown in Fig. 1i plotted against their respective mean enstrophy, $\bar{\Omega}$. The dashed line is the best linear fit. Error bars represent standard deviation. **d**, Relative tangential and radial components of velocity and speed of pairs of vortex–antivortex plotted as a function of distance. Each point averages pairs across 11 states at the same frame before annihilation (in total 6,224 annihilating pairs across 11 steady states). Error bars represent standard error. The shaded area denotes the transition of many-body to two-body interactions. **e**, Time-lapse snapshots of phase velocity field streamlines, coloured by circulation direction, in the vicinity of a pair of defects during an annihilation event. Scale bar, 2 μm. **f**, Mean pairwise distance and mean relative velocity of vortex–antivortex pairs plotted as a function of time before annihilation. The shaded regions represent standard deviation.

observation period (~100 s), the mean square displacement of the defects' motions scales approximately linearly with time (Extended Data Fig. 2a). In each individual experiment, we observe approximately the same numbers of positive and negative defects in the field of view (Extended Data Fig. 2b). Localized creation and annihilation events always involve pairs of oppositely charged defects (Fig. 1g and Supplementary Video 5), resulting in conservation of the total topological charge. Continual pair creation and annihilation causes the defect number density to fluctuate around a constant local mean value (Fig. 1h). Despite the differences in the spatiotemporal wave patterns, the fraction of creation and annihilation events (compared to total defect number) is ~10% in all states (Extended Data Fig. 2c,d) and defect lifetimes are exponentially distributed (Extended Data Fig. 2e). The local mean values of defect densities decrease for larger pattern wavelengths (Fig. 1i and Extended Data Fig. 3), consistent with previous reports for cortical maps[44]. These results point toward the possibility that generic mechanisms underlie defect dynamics in the biochemical signalling protein pattern on the membrane of the oocytes.

The local wavevector field, $\mathbf{V}_\phi(\mathbf{x}, t) = \nabla\phi(\mathbf{x}, t)$ is proportional to the velocity at which the information encoded in Rho-GTP concentration waves propagates on the 2D membrane (Fig. 2a(iii)). In analogy to 2D quantum superfluids in Bose–Einstein condensates[12,13,31,45], one can interpret $\mathbf{V}_\phi$ as an effective velocity field describing a potential flow with vorticity $\omega = \nabla \times \mathbf{V}_\phi$ localized at point-like vortex cores (Fig. 2a(iv)); in this framework, the Rho-GTP diffusion constant plays the role of $\hbar/m$ in quantum fluids to convert $\mathbf{V}_\phi$ to a velocity. The phase field defects of charge +1 or −1 map to centres of counterclockwise or clockwise vortices in the $\mathbf{V}_\phi$ field, respectively (Fig. 2a). The system exhibits turbulent behaviour, characterized by a weakly correlated distribution of a large number of vortices and antivortices of unit winding (Fig. 2a(iv)). We quantified the relative fraction of persistent dipole pairs for each steady state (Supplementary Video 6 and Methods). All steady states are characterized by a low fraction of bound vortex–antivortex pairs (~20%), reminiscent of the disordered phase in a Berezinskii, Kosterlitz and Thouless (BKT) topological phase transition (Fig. 2b)[46]. We did not observe evidence of same-sign clusters or super condensates in any of our experimental steady states (Extended Data Fig. 2f and Supplementary Video 6). A further analysis of the global properties of the phase gradient field, $\mathbf{V}_\phi$, reveals a linear scaling between the effective kinetic energy, $\bar{E} = \langle|\mathbf{V}_\phi|^2\rangle$, and effective enstrophy, $\bar{\Omega} = \langle\omega^2\rangle$ (Fig. 2c, Extended Data Fig. 4 and Methods), in agreement with recent reports for bacterial turbulence[15]. We next focus on the velocity statistics of the individual defects, which are significantly affected by vortex pair collisions. The analysis of radial and tangential components of the velocities of vortex pairs as a function of distance (before collision) reveals the length scale of transition from many-body to two-body interactions, ~5 μm (Fig. 2d), consistent with the length scale we extract from the linear relation between effective kinetic energy and effective enstrophy (Fig. 2c). By tracking pairs of nearby vortices on the oocyte membranes, we found that vortices accelerate substantially as their separation decreases and streamlines become compressed (Fig. 2e,f, Extended Data Fig. 5

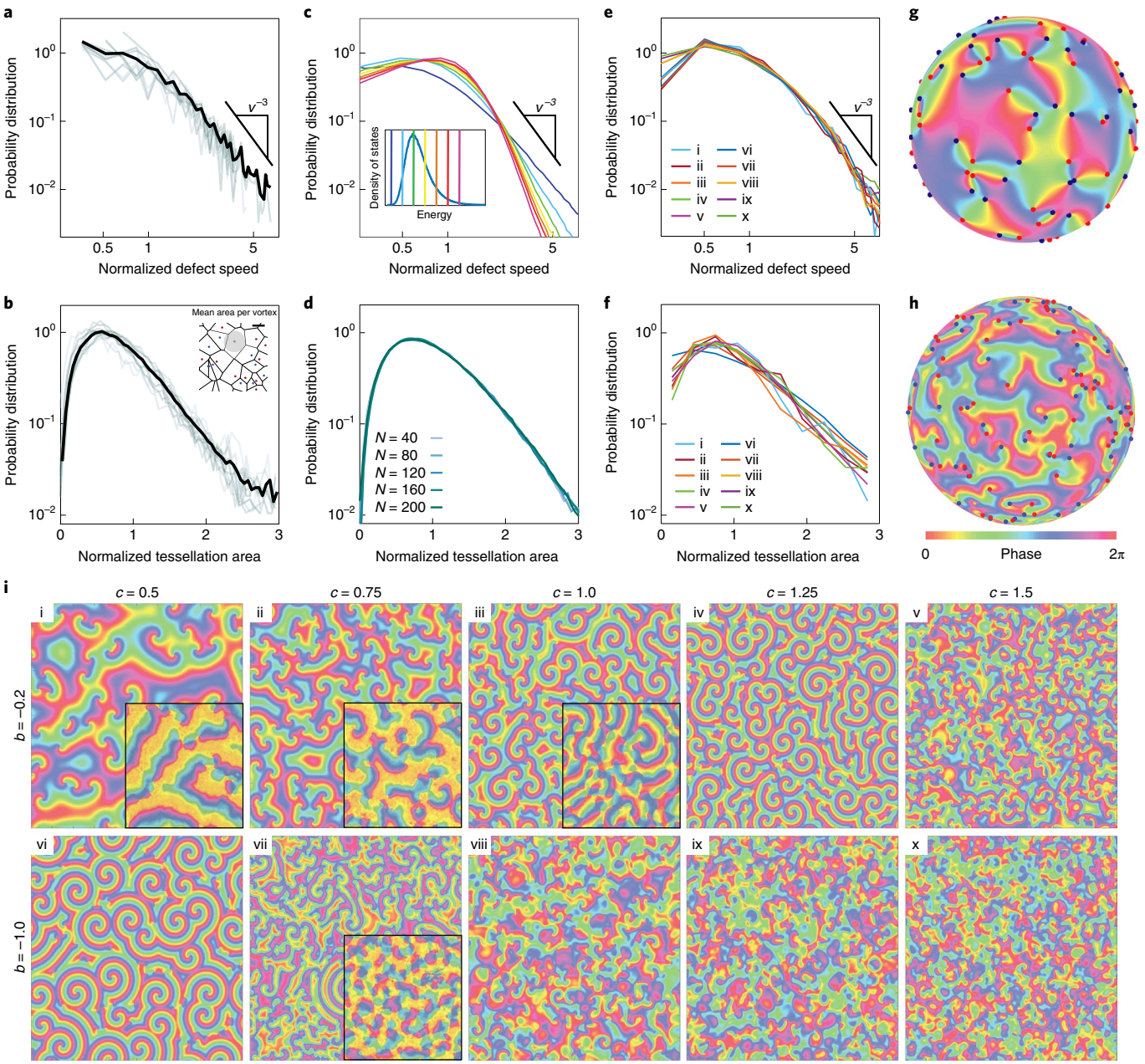

Fig. 3 | Comparison of the experimentally observed defect statistics with a discrete Helmholtz–Onsager point vortex model and a complex Ginzburg–Landau continuum model. a, Time-averaged defect speed distributions (normalized by their means) for the 11 states shown in Fig. 1i and their average (black line) are consistent with an asymptotic power-law behaviour. **b**, Time-averaged distributions of Voronoi areas around defects for the 11 states in Fig. 1i and their averaged distribution (black line) exhibit an approximately exponential tail. Inset: Voronoi tessellation for an observed vortex configuration and mean Voronoi vortex area (shaded) used to normalize the tessellation area across all states. Scale bar, 10 μm. **c**,**d**, Simulation results for the HO model on a sphere (see Methods). In **c**, vortex speed statistics ($N = 60$) exhibit power-law tails with exponents dependent on total energy. Inset (**c**): density of states for the model, calculated via a Monte Carlo simulation with 10^6 samples. Vertical lines are placed at energies corresponding to plotted speed statistics. In **d**, Voronoi area distributions for the light blue total energy (subcritical) collapse when normalized by vortex density (see also Extended Data Fig. 7). **e**,**f**, Simulation results for the CGL model on a sphere. **g**,**h**, Although the reconstructed phase field for the near-field HO model (**g**) differs from that of the CGL model (**h**), both models show defect area statistics (**d**,**f**) similar to the experiments (**b**). **i**, The experimentally observed wave patterns (insets) can be mapped onto specific states in the CGL phase diagram (see also Extended Data Fig. 8). Parameters b and c characterize the linear and nonlinear dispersion.

and Supplementary Video 5). Such encounters and annihilation events give rise to a noticeable tail in the experimentally measured defect speed distributions (Fig. 3a). At high velocities, these tails decay approximately as v^{-3}, in agreement with recent theoretical predictions for generic vortex interactions[47,48]. To characterize the vortex size statistics, we constructed a Voronoi tessellation centred around the topological defects in the phase field (Fig. 3b and Extended Data Fig. 6). The experimentally measured area distributions of the Voronoi cells exhibit an exponential decay, as also predicted recently for turbulent active nematics[7]. Taken together, our data suggest that

essential aspects of the defect statistics characterizing the complex dynamics of membrane Rho-GTP waves on the oocyte membrane can be understood in terms of generic 2D defect–defect interactions.

To further test this hypothesis, we compared our experimental results with simulations of the discrete Helmholtz–Onsager (HO) point-vortex model[21] and a complex Ginzburg–Landau (CGL) continuum theory[22]. The CGL model presents a generic continuum theory to describe nonlinear waves and defect turbulence in non-equilibrium systems[31], and can be derived from a simplified Rho-GTP reaction-kinetics model (Supplementary Information). The HO model provides a widely studied minimal Hamiltonian dynamics framework for 2D vortex motions[11] with logarithmic pair interaction potential. Mathematically, it is directly related to solutions of the Euler equations describing 2D classical turbulence, and it has been successfully applied recently to describe the experimentally observed vortex dynamics in 2D Bose–Einstein condensates[31]. Relevant to the parameter regime realized in our experiments (see Supplementary Information), the HO model also provides a near-field approximation (see Supplementary Information) to the CGL spiral defect dynamics[49].

We simulated both models by approximating the oocyte surface with a spherical domain. For the HO model, we numerically solved the Hamiltonian equations of motion[50] of N vortices with circulations $\Gamma_i = \pm 1$, and transformed the simulation data into phase field data (Fig. 3g, Extended Data Fig. 7 and Methods). Simulations of the CGL model directly yield the phase field from the polar representation of the complex order parameter (Fig. 3h and Methods). By performing numerical parameter scans, we mapped the experimentally observed wave patterns to the corresponding states in the CGL phase diagram (Fig. 3i, Extended Data Fig. 8 and Supplementary Information).

A comparison with the experimentally measured phase fields shows that the best-fit CGL models reproduce essential aspects of the spiral wave morphology of the Rho-GTP waves (Fig. 3i). By contrast, the near-field HO description cannot account for details of the spiral wave morphology (Fig. 3g). Nevertheless, both models exhibit defect vortex speed statistics (Fig. 3c,e) and Voronoi tessellation area statistics (Fig. 3d,f) similar to those observed in our experiments (Fig. 3a,b). Test simulations replacing the logarithmic HO potential with a Bessel function, as typically used to describe intermediate- to-long-range spiral core interactions[49,51], also yielded similar statistics (Extended Data Fig. 9 and Supplementary Information). The tails of the defect speed distributions for the HO point-vortex model depend on the total energy in the system (Fig. 3c), whereas the CGL model displays nearly identical vortex speed statistics when the complex diffusion parameter is varied in the defect-mediated turbulence regime (Fig. 3e and Methods). Within the limitations of our microscope field of view and resolution, the approximately cubic asymptotic decay observed both in the experiments (Fig. 3a) and CGL simulations (Fig. 3e) agrees with recent theoretical predictions for random point-vortex configurations[52]. For the HO model (Fig. 3c), slopes close to v^{-3} are found only for subcritical to critical energies below the vortex condensation transition, consistent with the observation of weak BKT-type dipole signatures[46] in our experimental vortex tracking data (Fig. 2b, Extended Data Fig. 2f and Supplementary Video 6). In the experiments as well as simulations, the distributions of the Voronoi cell areas collapse after normalization by the mean area, and their tails show an approximately exponential decay (Fig. 3b,d,f and Extended Data Fig. 10), in agreement with predictions for defect turbulence in active nematics[7]. Taken together, the statistics observed in the experiments and CGL simulations support the hypothesis that the Rho-GTP dynamics on the 2D oocyte membrane realizes a state of defect-mediated turbulence[22]. The turbulent non-equilibrium dynamics on the 2D membrane is maintained by an active energy input from the underlying bulk cytoplasm[20] in the form of adenosine triphosphate (ATP) and GTP hydrolysis. Conceptually, this ATP/GTP-mediated driving process plays a role similar to that of Gaussian or spectral forcing in 2D atmospheric turbulence[53].

In conclusion, our results reveal interesting parallels between the phase field defects in Rho-GTP concentration waves on the starfish oocyte membrane, generic Ginzburg–Landau theories and point vortices in 2D Bose–Einstein condensates[12,31]. A future challenge will be to investigate whether biochemical signalling systems can intrinsically or externally (for example, with optogenetic tools for light activation of Rho-GTP regulatory proteins) be driven close to, or even past, the critical phase transition regime that separates low-energy turbulent spiral-vortex dynamics from high-energy vortex condensation[46]. From a broader conceptual perspective, it will be intriguing to explore further the similarities and differences between topological defect dynamics and information propagation in living and non-living systems.

Online content

Any methods, additional references, Nature Research reporting summaries, source data, extended data, supplementary information, acknowledgements, peer review information; details of author contributions and competing interests; and statements of data and code availability are available at https://doi.org/10.1038/s41567-020-0841-9.

Received: 21 February 2019; Accepted: 17 February 2020;
Published online: 23 March 2020

References

1. Gray, R. A., Pertsov, A. M. & Jalife, J. Spatial and temporal organization during cardiac fibrillation. *Nature* **392**, 75–78 (1998).
2. Witkowski, F. X. et al. Spatiotemporal evolution of ventricular fibrillation. *Nature* **392**, 78–82 (1998).
3. Christoph, J. et al. Electromechanical vortex filaments during cardiac fibrillation. *Nature* **555**, 667–672 (2018).
4. Huang, X. Y. et al. Spiral wave dynamics in neocortex. *Neuron* **68**, 978–990 (2010).
5. Saw, T. B. et al. Topological defects in epithelia govern cell death and extrusion. *Nature* **544**, 212–216 (2017).
6. Sanchez, T., Chen, D. T., DeCamp, S. J., Heymann, M. & Dogic, Z. Spontaneous motion in hierarchically assembled active matter. *Nature* **491**, 431–434 (2012).
7. Giomi, L. Geometry and topology of turbulence in active nematics. *Phys. Rev. X* **5**, 031003 (2015).
8. Nishiguchi, D., Aranson, I. S., Snezhko, A. & Sokolov, A. Engineering bacterial vortex lattice via direct laser lithography. *Nat. Commun.* **9**, 4486 (2018).
9. Musevic, I., Skarabot, M., Tkalec, U., Ravnik, M. & Zumer, S. Two-dimensional nematic colloidal crystals self-assembled by topological defects. *Science* **313**, 954–958 (2006).
10. Scheeler, M. W., van Rees, W. M., Kedia, H., Kleckner, D. & Irvine, W. T. M. Complete measurement of helicity and its dynamics in vortex tubes. *Science* **357**, 487–490 (2017).
11. Eyink, G. L. & Sreenivasan, K. R. Onsager and the theory of hydrodynamic turbulence. *Rev. Mod. Phys.* **78**, 87–135 (2006).
12. Anderson, B. P. Resource article: experiments with vortices in superfluid atomic gases. *J. Low Temp. Phys.* **161**, 574–602 (2010).
13. Fetter, A. L. Vortices and dynamics in trapped Bose–Einstein condensates. *J. Low Temp. Phys.* **161**, 445–459 (2010).
14. Bradley, A. S. & Anderson, B. P. Energy spectra of vortex distributions in two-dimensional quantum turbulence. *Phys. Rev. X* **2**, 041001 (2012).
15. Dunkel, J. et al. Fluid dynamics of bacterial turbulence. *Phys. Rev. Lett.* **110**, 228102 (2013).
16. Wu, K. T. et al. Transition from turbulent to coherent flows in confined three-dimensional active fluids. *Science* **355**, eaal1979 (2017).
17. Lechleiter, J., Girard, S., Peralta, E. & Clapham, D. Spiral calcium wave-propagation and annihilation in *Xenopus laevis* oocytes. *Science* **252**, 123–126 (1991).
18. Lechleiter, J. D. & Clapham, D. E. Spiral waves and intracellular calcium signaling. *J. Physiol.* **86**, 123–128 (1992).
19. Etienne-Manneville, S. & Hall, A. Rho GTPases in cell biology. *Nature* **420**, 629–635 (2002).
20. Bement, W. M. et al. Activator–inhibitor coupling between Rho signaling and actin assembly makes the cell cortex an excitable medium. *Nat. Cell Biol.* **17**, 1471–1483 (2015).

21. Onsager, L. Statistical hydrodynamics. *Nuovo Cim.* **6**, 279–287 (1949).
22. Aranson, I. S. & Kramer, L. The world of the complex Ginzburg–Landau equation. *Rev. Mod. Phys.* **74**, 99–143 (2002).
23. Kraichnan, R. H. & Montgomery, D. Two-dimensional turbulence. *Rep. Prog. Phys.* **43**, 547–619 (1980).
24. Mermin, N. D. The topological theory of defects in ordered media. *Rev. Mod. Phys.* **51**, 591–648 (1979).
25. Moffatt, H. K. Degree of knottedness of tangled vortex lines. *J. Fluid Mech.* **35**, 117–129 (1969).
26. Kleckner, D. & Irvine, W. T. M. Creation and dynamics of knotted vortices. *Nat. Phys.* **9**, 253–258 (2013).
27. Paulose, J., Chen, B. G. G. & Vitelli, V. Topological modes bound to dislocations in mechanical metamaterials. *Nat. Phys.* **11**, 153–156 (2015).
28. Keber, F. C. et al. Topology and dynamics of active nematic vesicles. *Science* **345**, 1135–1139 (2014).
29. Fyfe, D. & Montgomery, D. High-beta turbulence in two-dimensional magnetohydrodynamics. *J. Plasma Phys.* **16**, 181–191 (2009).
30. Zwierlein, M. W., Abo-Shaeer, J. R., Schirotzek, A., Schunck, C. H. & Ketterle, W. Vortices and superfluidity in a strongly interacting Fermi gas. *Nature* **435**, 1047–1051 (2005).
31. Gauthier, G. et al. Giant vortex clusters in a two-dimensional quantum fluid. *Science* **364**, 1264–1267 (2019).
32. Kawaguchi, K., Kageyama, R. & Sano, M. Topological defects control collective dynamics in neural progenitor cell cultures. *Nature* **545**, 327–331 (2017).
33. Epstein, I. R. & Pojman, J. A. *An Introduction to Nonlinear Chemical Dynamics: Oscillations, Waves, Patterns, and Chaos* (Oxford Univ. Press, 1998).
34. Halatek, J. & Frey, E. Rethinking pattern formation in reaction–diffusion systems. *Nat. Phys.* **14**, 507–514 (2018).
35. Petrov, V., Gaspar, V., Masere, J. & Showalter, K. Controlling chaos in the Belousov–Zhabotinsky reaction. *Nature* **361**, 240–243 (1993).
36. Jakubith, S., Rotermund, H. H., Engel, W., Vonoertzen, A. & Ertl, G. Spatiotemporal concentration patterns in a surface-reaction: propagating and standing waves, rotating spirals, and turbulence. *Phys. Rev. Lett.* **65**, 3013–3016 (1990).
37. Hildebrand, M., Bar, M. & Eiswirth, M. Statistics of topological defects and spatiotemporal chaos in a reaction-diffusion system. *Phys. Rev. Lett.* **75**, 1503–1506 (1995).
38. Totz, J. F., Rode, J., Tinsley, M. R., Showalter, K. & Engel, H. Spiral wave chimera states in large populations of coupled chemical oscillators. *Nat. Phys.* **14**, 282–285 (2018).
39. Coullet, P., Gil, L. & Lega, J. Defect-mediated turbulence. *Phys. Rev. Lett.* **62**, 1619–1622 (1989).
40. Sawai, S., Thomason, P. A. & Cox, E. C. An autoregulatory circuit for long-range self-organization in Dictyostelium cell populations. *Nature* **433**, 323–326 (2005).
41. Reeves, M. T., Anderson, B. P. & Bradley, A. S. Classical and quantum regimes of two-dimensional turbulence in trapped Bose–Einstein condensates. *Phys. Rev. A* **86**, 053621 (2012).
42. Neely, T. W. et al. Characteristics of two-dimensional quantum turbulence in a compressible superfluid. *Phys. Rev. Lett.* **111**, 235301 (2013).
43. Marchetti, M. C. et al. Hydrodynamics of soft active matter. *Rev. Mod. Phys.* **85**, 1143 (2013).
44. Lee, H. Y., Yahyanejad, M. & Kardar, M. Symmetry considerations and development of pinwheels in visual maps. *Proc. Natl Acad. Sci. USA* **100**, 16036–16040 (2003).
45. Billam, T. P., Reeves, M. T., Anderson, B. P. & Bradley, A. S. Onsager–Kraichnan condensation in decaying two-dimensional quantum turbulence. *Phys. Rev. Lett.* **112**, 145301 (2014).
46. Yu, X. Q., Billam, T. P., Nian, J., Reeves, M. T. & Bradley, A. S. Theory of the vortex-clustering transition in a confined two-dimensional quantum fluid. *Phys. Rev. A* **94**, 023602 (2016).
47. Bray, A. J. Velocity distribution of topological defects in phase-ordering systems. *Phys. Rev. E* **55**, 5297–5301 (1997).
48. Angheluta, L., Jeraldo, P. & Goldenfeld, N. Anisotropic velocity statistics of topological defects under shear flow. *Phys. Rev. E* **85**, 011153 (2012).
49. Aguareles, M., Chapman, S. J. & Witelski, T. Motion of spiral waves in the complex Ginzburg–Landau equation. *Phys. D* **239**, 348–365 (2010).
50. Dritschel, D. G. & Boatto, S. The motion of point vortices on closed surfaces. *Proc. R. Soc. A* **471**, 20140890 (2015).
51. Rica, S. & Tirapegui, E. Dynamics of defects in the complex Ginzburg–Landau equation. *Phys. D* **61**, 246–252 (1992).
52. Skaugen, A. & Angheluta, L. Velocity statistics for nonuniform configurations of point vortices. *Phys. Rev. E* **93**, 042137 (2016).
53. Boffetta, G. & Ecke, R. E. Two-dimensional turbulence. *Annu. Rev. Fluid Mech.* **44**, 427–451 (2012).

Methods

Starfish oocyte preparation. *Patiria miniata* starfish were procured from South Coast Bio-Marine. The animals were kept in a salt-water fish tank maintained at 15 °C. The ovaries were extracted through a small incision made at the bottom of the starfish. The ovaries were carefully fragmented using a pair of scissors to release the oocytes. Extracted oocytes were washed twice with calcium-free seawater to prevent maturation and incubated in filtered seawater at 15 °C. Our dataset includes seven oocytes from two different batches. All experiments were performed within three days of oocyte extraction.

In vitro synthesis of mRNA and microinjection. Two constructs were used in this study. The fluorescently labelled rhotekin binding domain construct, eGFP-rGBD, was purchased from Addgene, deposited by William Bement[54]. The fluorescently labelled Ect2-T808A-mCherry construct, a mutant that is desensitized to one particular Cdk1 phosphorylation, which otherwise limits membrane association during the M-phase, was a gift from G. von Dassow. For in vitro synthesis of mRNA, we first amplified the constructs by bacterial growth overnight. The plasmids were then purified using Miniprep (Qiagen) and linearized using the appropriate restriction enzymes. Both eGFP-rGBD and Ect2-T808A-mCherry mRNA were synthesized using the SP6 mMessage mMachine transcription kits (Thermo Fisher Scientific). To express the constructs, the synthesized mRNA was microinjected into the cytoplasm of the oocytes and incubated overnight at 15 °C.

PDMS chamber. Microfabricated chambers were fabricated by casting gas-permeable PDMS onto patterned silicon wafers. The chamber shapes were designed with a height of 80 µm and surface area of ~27,000 µm², to match typical volumes of the oocytes. The patterned silicon wafer was manufactured using photolithography (Microfactory SAS). The silicon wafer was silanized with trichlorosilane (Sigma 448931). PDMS was made by mixing Dow SYLGARD 184 Silicone Elastomer Clear solution at a 10:1 base-to-curing agent ratio. After mixing thoroughly, the elastomer was poured over the silicon master mould, degassed in a vacuum chamber and cured at 60 °C in oven for an hour.

Confocal imaging. Fluorescence imaging of rGBD-GFP was performed on a Zeiss 700 laser scanning confocal system. The system consisted of a Zeiss AxioObserver motorized inverted microscope stand and three photomutiplier detectors. Images were acquired using a ×40/NA 1.3 oil Plan Apochromat objective with appropriate laser line and emission filter, in a microscope room maintained at 20–22 °C.

Calculation of the phase field. We constructed the full phase field $\phi(\mathbf{x}, t)$ by calculating the phase at each individual pixel as a function of time, $\phi(t)$, over the entire 2D video image parameterized by $\mathbf{x}$. The fluorescence intensity time series at single pixels $I(t)$ is oscillatory. The phase can be determined by plotting the 2D phase portrait of $I(t+\tau)$ versus $I(t)$ (Extended Data Fig. 1b)[1]. To correct for varying background intensity, we defined the mean subtracted signal as $\tilde{I}(t) = I(t) - \bar{I}(t)$. $\bar{I}(t)$ is the mean intensity calculated over a sliding window of length $w = 15$. The phase is then computed as $\phi(t) = \tan^{-1}(\tilde{I}(t+\tau), \tilde{I}(t))$. We chose τ to be approximately a quarter of the signal's wave period. To smooth out the noise, we applied a Gaussian filter with a radius of one pixel to obtain the final phase field.

Calculation of normalized intensity cross-correlation and pattern wavelength. The normalized intensity cross-correlation $C(R)$, as a function of the two-point distance R, was calculated from $C(R)_T = \langle \hat{I}(\mathbf{x}_i) \cdot \hat{I}(\mathbf{x}_j) \rangle / (\sigma_{\hat{I}(\mathbf{x}_i)} \cdot \sigma_{\hat{I}(\mathbf{x}_j)})$ for time T throughout the steady state. Pixel position pairs $(\mathbf{x}_i, \mathbf{x}_j)$ satisfying $|\mathbf{x}_i - \mathbf{x}_j| = R$ were collected by first randomly selecting 1,000 pixels on the x–y plane as $\mathbf{x}_i$, then gathering all the pixels that fall on the ring centred at $\mathbf{x}_i$ with radius R as $\mathbf{x}_j$. Pixel intensity values of the pairs, $\hat{I}(\mathbf{x}_i), \hat{I}(\mathbf{x}_j)$, were acquired from background subtracted images (see section 'Background subtraction'). The intensity cross-correlation was normalized by the standard deviation of sampled intensity value collections, $\sigma_{\hat{I}(\mathbf{x}_i)}$ and $\sigma_{\hat{I}(\mathbf{x}_j)}$. Discontinuous two-pixel distance R was sorted into 1 µm bins when plotting $C(R)$ in Fig. 1c and Extended Data Fig. 3a. The wavelength extracted from patterns at time T (Extended Data Fig. 3b) was defined as the position of the first peak in the $C(R)_T$ curve.

Calculation of energy spectrum and pattern wavenumber. Energy spectrum $E(\mathbf{k})_T$ at every time T was also calculated from the intensity field $\hat{I}(\mathbf{x})$ (see section 'Background subtraction'). 2D fast Fourier transformation of $\hat{I}(\mathbf{x})$, $S(\mathbf{k})$, was calculated using MATLAB function '*fft2*' for the max square region centred at each pattern. The energy spectrum $E(\mathbf{k})$ is given by $E(\mathbf{k}) = S^*(\mathbf{k})S(\mathbf{k})$. The zero wavenumber value in $E(\mathbf{k})$ was removed (Extended Data Fig. 3c). The 1D energy spectrum $p(k)$ was calculated by integrating along the angular direction: $p(k) = \sum_{\mathbf{k}'} E(\mathbf{k}')\delta(|\mathbf{k}'| = k)$. We defined the characteristic wavenumber as the mean wavenumber weighted by normalized 1D energy spectrum, $\bar{k} = \int_0^{k_0} k \cdot p(k)\mathrm{d}k / \int_0^{k_0} p(k)\mathrm{d}k$. Wavenumber cutoff was set to 0.2 µm^{-1} for all patterns (Extended Data Fig. 3d).

Background subtraction. A mean intensity value $\langle I \rangle = \langle I(\mathbf{x}, t) \rangle_{\mathbf{x},t}$ was subtracted from every video. The background subtracted intensity field $\hat{I}(\mathbf{x}, t) = I(\mathbf{x}, t) - \langle I \rangle$ was used in calculating the characteristic pattern wavelength and wavenumber. For data sets with significant spatially extended bright fluorescence patches (2 out of 11), we invert the intensity field to more accurately extract the length scale. The background subtracted intensity field $\hat{I}'(\mathbf{x})$ was then defined as $\hat{I}'(\mathbf{x}) = \max(\hat{I}_0 - \hat{I}(\mathbf{x}), 0)$, where $\hat{I}_0$ is the mean intensity of fluorescence at the edge of bright patches.

Determination and tracking of phase singularity. To determine the position of the phase singularities, we scanned through the entire image and computed the line integral $\oint \nabla\phi(\mathbf{x}) \cdot \mathbf{ds}$ for every two-by-two local window. Plus (minus) phase singularities have a value of 2π (-2π). We identified the positions of the phase singularities independently in each time frame. Once the phase singularities were obtained, the trajectories were constructed using particle tracking software with a gap-closing algorithm (developed by J.-Y. Tinevez). The software is based on the Munkres/Hungarian algorithm and is available from the FileExchange on the MathWorks website (https://www.mathworks.com/matlabcentral/fileexchange/34040-simple-tracker).

Calculation of phase velocity, vorticity, effective kinetic energy and effective enstrophy. The phase velocity was calculated by taking the gradient of the phase field $\mathbf{V}_\phi(\mathbf{x}, t) = \nabla\phi(\mathbf{x}, t)$. Vorticity $\omega(\mathbf{x}, t) = \nabla \times \mathbf{V}_\phi(\mathbf{x}, t)$ was computed using MATLAB's curl function. The effective kinetic energy was calculated by averaging over all phase velocities squared $\bar{E} = \left\langle \left| \mathbf{V}_\phi(\mathbf{x}, t) \right|^2 \right\rangle$. Here, $\langle \dots \rangle$ denotes a spatial and temporal average. Effective enstrophy was calculated by averaging over all vorticities squared $\bar{\Omega} = \left\langle \left| \omega(\mathbf{x}, t) \right|^2 \right\rangle$. Although the spatial averages $E(t)$ and $\Omega(t)$ fluctuate, their time averages $\bar{E}$ and $\bar{\Omega}$ are approximately constant over the time interval used in data analysis (Extended Data Fig. 4). Streamline visualization of the phase velocity field was realized using the Python software package 'Streamplot' available in matplotlib library[55].

Determination of dipole pairs and clusters. We first categorized all defects into dipole, cluster or free vortex state using the clustering algorithm outlined in ref. [56]. Briefly, at each time frame, defects can be categorized as one of three cases:

1. Dipole, if a pair of +1 and −1 defects are mutual nearest (opposite-sign) neighbours
2. Cluster, if there exist same-sign neighbours that are nearer than the nearest opposite-sign neighbour
3. Free vortex, if the nearest opposite-sign neighbour belongs to another dipole or cluster and there are no same-sign neighbours that are nearer

To calculate the relative fraction of persistent dipole pairs, we only consider dipole pairs that persist for three frames or more.

Distribution of normalized instantaneous speeds. Instantaneous defect speed was calculated as $v(t) = |\mathbf{x}(t) - \mathbf{x}(t - \Delta t)|/\Delta t$, with Δt being the video's time resolution. An ensemble of defect velocities was constructed by taking every instantaneous $v(t)$ of all defect trajectories over the entire video. The normalized speed was computed by scaling the defect speed with the mean value of the ensemble, $\tilde{v} = v/\bar{v}$. The normalized speed distribution $P(\tilde{v})$ was then plotted using MATLAB's histogram function for every steady-state pattern. The distributions of the 11 states (Fig. 3a) were plotted by averaging the values of $P(\tilde{v})$ within each $\tilde{v}$ bin. The power-law scaling spanning across $\tilde{v}$ from 0.1 to 6.5 is robust against changes in binning width $\Delta\tilde{v}$.

Calculation of the relative velocity between a pair of vortices. We characterized annihilation events by identifying pairs of oppositely charged vortices that disappeared simultaneously between the same two frames and had their last observed locations within 10 pixels in distance. The time zero (Fig. 2d,e and Extended Data Fig. 5) for the annihilation events was defined as the last observed frame of annihilating pair vortices. At every time point t, the relative speed between pair vortices was computed from the positions of the current frame and the frame before, $v_{\mathrm{rel}}(t) = |(\mathbf{x}^+(t) - \mathbf{x}^+(t - \Delta t)) - (\mathbf{x}^-(t) - \mathbf{x}^-(t - \Delta t))|/\Delta t$. Pairwise distance was calculated from the position of the current frame, $d(t) = |(\mathbf{x}^+(t) - \mathbf{x}^-(t))|$. Radial relative velocity was defined such that the radial velocity is positive if it points to a decrease of pairwise distance; tangential relative velocity was defined such that counterclockwise rotating tangential velocity is positive (Fig. 2d, inset).

Voronoi tessellation area distributions. We used the default MATLAB function 'voronoin' in the 'Computational Geometry' toolbox to calculate Voronoi tessellations of point vortices at every time frame. Only tessellations with edges not crossing the boundary of the steady-state pattern were used to calculate area statistics. We computed the probability distribution in Fig. 3b using all tessellation areas throughout every steady-state pattern. For each pattern, the normalized tessellation area was computed by multiplying by the pattern's time-averaged vortex area density. This is effectively normalizing the tessellation area by the mean area taken up by a single vortex (Fig. 3b, inset). The combined distribution was

calculated by averaging histogram counts inside each normalized area bin for the 11 steady states.

Onsager model simulations. The Onsager, or point-vortex, model is a simplified Hamiltonian model of interacting vortices in two dimensions[11]. The state of the system is entirely determined by the positions of N vortices, with two spatial degrees of freedom for each vortex conjugate pair. To be topologically consistent, a variant of the model embedded on the surface of a unit sphere was chosen[50]. Under these conditions, vortex–vortex interactions are logarithmic, with the Hamiltonian given as

$$H = -\frac{1}{4\pi}\sum_{j\neq k}\Gamma_j\Gamma_k \log\left(\frac{|\mathbf{x}_k - \mathbf{x}_j|}{2}\right) + \text{const.}$$

where $|\mathbf{x}_k - \mathbf{x}_j|$ refers to the chord distance in $\mathbb{R}^3$. The constant term varies with the circulation strength Γ_i and with N, but is independent of the specific configuration and thus does not influence the dynamics. The equations of motion for the kth particle are given as

$$\dot{\mathbf{x}}_k = \frac{1}{4\pi}\sum_{j\neq k}\Gamma_j \frac{\mathbf{x}_j \times \mathbf{x}_k}{1 - \mathbf{x}_j \cdot \mathbf{x}_k}$$

Simulations were performed by numerically integrating via a fourth-order Runge–Kutta scheme, based on a publicly available MATLAB implementation[57]. In all simulations, vortex circulations Γ_i are evenly split between +1 and −1. Each vortex is assigned an initial position at random based on a uniform distribution over the surface of the sphere. To create a simulation with a desired total energy E_0, random initial conditions were continually sampled until a configuration with $|E - E_0| < 0.1$ was produced. From initiation, the system was evolved for $T = 1{,}000$ according to the equations of motion, with $\mathrm{d}t = 0.01$.

CGL simulations. The CGL is a universal model describing the spatiotemporal evolution of continuum systems near the critical point of a Hopf bifurcation. Among its many applications, it has been widely used in the study of wave behaviour in reaction–diffusion systems[22]. The basic form of the equations is

$$\partial_t A = D(1 + ib)\nabla^2 A + A - (1 + ic)|A|^2 A$$

We simulated the behaviour of this system on the unit sphere using the open-source Spherefun library[58]. For the simulations shown in the Extended Data Fig. 8, we chose $D = 10^{-4}$, while b and c were varied to explore a variety of different spiral wave regimes. In all simulations, we used a time step of $\mathrm{d}t = 0.1$ and $N = 256$ grid points (see Spherefun documentation for details[58]). Simulations were begun with random initial conditions, and each lasted until $T = 4{,}000$, which in all cases was sufficient to ensure the emergence of a steady state.

Pattern matching between CGL and experimental data. To systematically compare the experimental and numerical results in Fig. 3i, the following procedure was employed. For each point in the CGL parameter space, a simulation was run on a 500 × 500 grid until steady state was reached. Via Fourier transform, the 2D k-space representation of the CGL phase field $\tilde{\phi}(k_x, k_y)$ was calculated. From this field, we calculated a series of 20 moments, defined as

$$M^{\text{simulation},i}_{n_x,n_y} = \left[\frac{1}{\phi_0}\int k_x^{n_x} k_y^{n_y} |\tilde{\phi}(k_x, k_y)| \mathrm{d}k_x \mathrm{d}k_y\right]^{\frac{1}{n_x+n_y}}$$

where the normalization factor is given by $\phi_0 = \int \tilde{\phi}(k_x, k_y)\mathrm{d}k_x\mathrm{d}k_y$. Via the same procedure, equivalent moments $M^{\text{experiment},j}_{n_x,n_y}$ were calculated for each of the 11 experimental steady states previously analysed. To calculate which CGL simulation most closely matched the experimental state, we calculated a fitting score defined as

$$f_{ij} = \sum_{n_x,n_y}\left|\frac{M^{\text{simulation},i}_{n_x,n_y}}{M^{\text{experiment},j}_{n_x,n_y}} - 1\right|$$

In Fig. 3i, and in Extended Data Fig. 8, each experiment is matched with the simulation which minimized the above scoring function.

Reporting Summary. Further information on research design is available in the Nature Research Reporting Summary linked to this Article.

Data availability

All data that support the plots within this paper and other findings of this study are available from the corresponding authors upon reasonable request.

Code availability

The algorithms and simulations codes are described in the Methods and Supplementary Information.

References

54. Benink, H. A. & Bement, W. M. Concentric zones of active RhoA and Cdc42 around single cell wounds. *J. Cell Biol.* **168**, 429–439 (2005).
55. Hunter, J. D. Matplotlib: a 2D graphics environment. *Comput. Sci. Eng.* **9**, 90–95 (2007).
56. Valani, R. N., Groszek, A. J. & Simula, T. P. Einstein–Bose condensation of Onsager vortices. *New J. Phys.* **20**, 053038 (2018).
57. Ashbee, T. *Point Vortex Dynamics Simulation* (MATLAB Central File Exchange, accessed 31 August 2018); https://www.mathworks.com/matlabcentral/fileexchange/49103-point-vortex-dynamics-simulation
58. Townsend, A., Wilber, H. & Wright, G. B. Computing with functions in spherical and polar geometries I. The sphere. *SIAM J. Sci. Comput.* **38**, C403–C425 (2016).

Acknowledgements

We thank M. Zwierlein, M. Kardar, H. Kedia and N. Goldenfeld for helpful discussions. This research was supported by a Sloan Research Fellowship (N.F.), a National Science Foundation CAREER Award (N.F.), a James S. McDonnell Foundation Complex Systems Scholar Award (J.D.) and the MIT Solomon Buchsbaum Research Fund (J.D.).

Author contributions

N.F. and J.D. designed and supervised the research. T.H.T. and M.T. performed experiments. J.L., T.H.T. and M.T. analysed the data. P.W.M. performed simulations. All authors discussed the experiment and simulation results and wrote the paper.

Competing interests

The authors declare no competing interests.

Additional information

Extended data is available for this paper at https://doi.org/10.1038/s41567-020-0841-9.

Supplementary information is available for this paper at https://doi.org/10.1038/s41567-020-0841-9.

Correspondence and requests for materials should be addressed to J.D. or N.F.

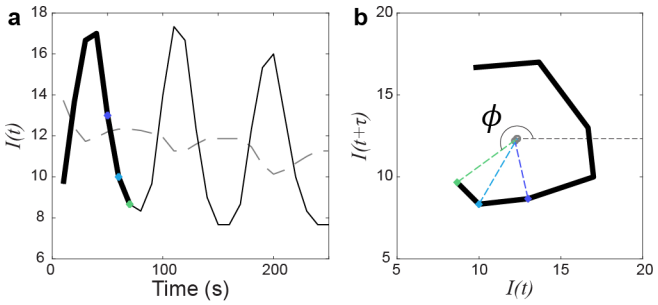

Extended Data Fig. 1 | Visualization of phase determination at single pixel level. a, Fluorescence intensity at each individual pixel, $I(t)$ is oscillatory. The gray dotted line is the mean intensity $\bar{I}(t)$. **b**, Phase from oscillation can be determined by plotting the two dimensional phase portrait of $I(t+\tau)$ versus $I(t)$. See Methods for more details.

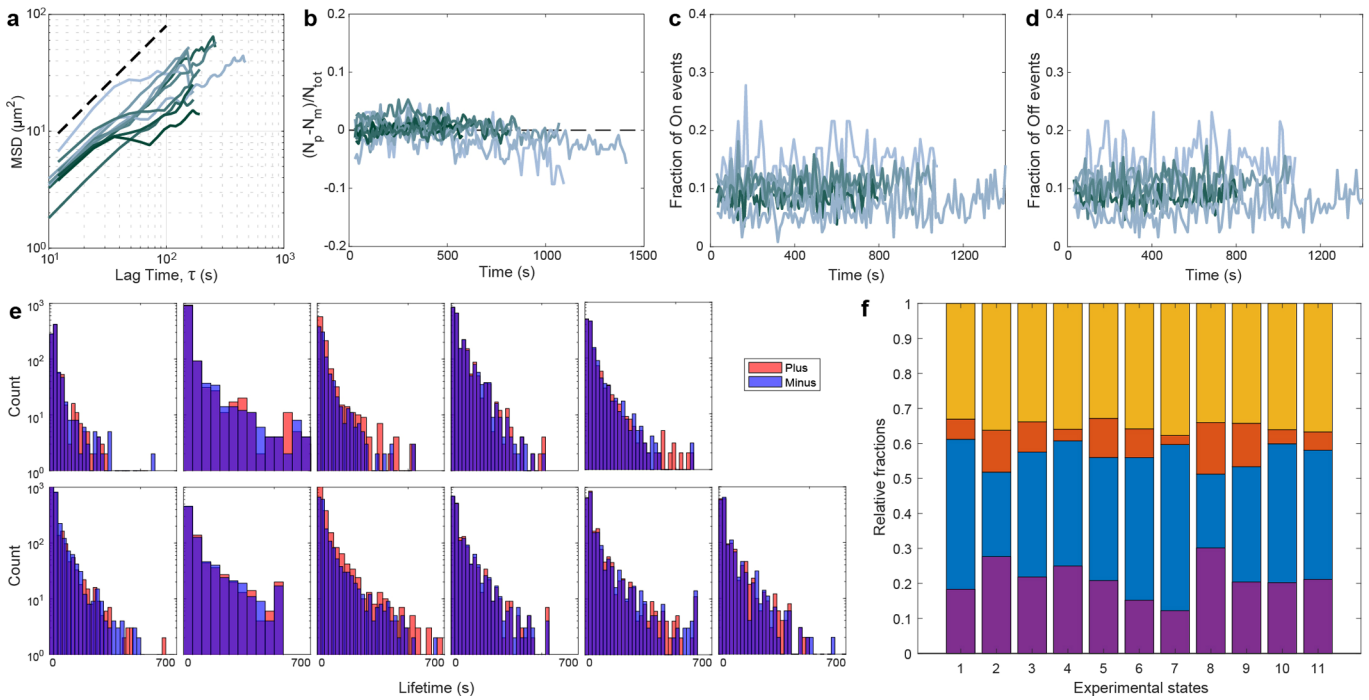

Extended Data Fig. 2 | Statistical characterization of defect dynamics. a, Mean squared displacement of defects plotted as a function of lag time τ. Dotted line has a slope of 1. **b**, Defect charge imbalance, quantified using the metric $(N_p-N_m)/N_t$, is plotted as a function of time. Here, N_p, N_m, and N_t denotes the number of +1, -1, and total defect respectively. **(c,d)**, Fraction of creation (on, **c**) and annihilation (off, **d**) events normalized by total defect number N_{on}/N_t and N_{on}/N_t plotted as a function of time for all 11 states. **e**, Distribution of +1 and -1 defects lifetime for all 11 states. **f**, Relative fractions of persistent dipole (purple), transient dipole (blue), cluster (orange) and free vortex (yellow) for all 11 states identified according to the clustering algorithm as described in Methods.

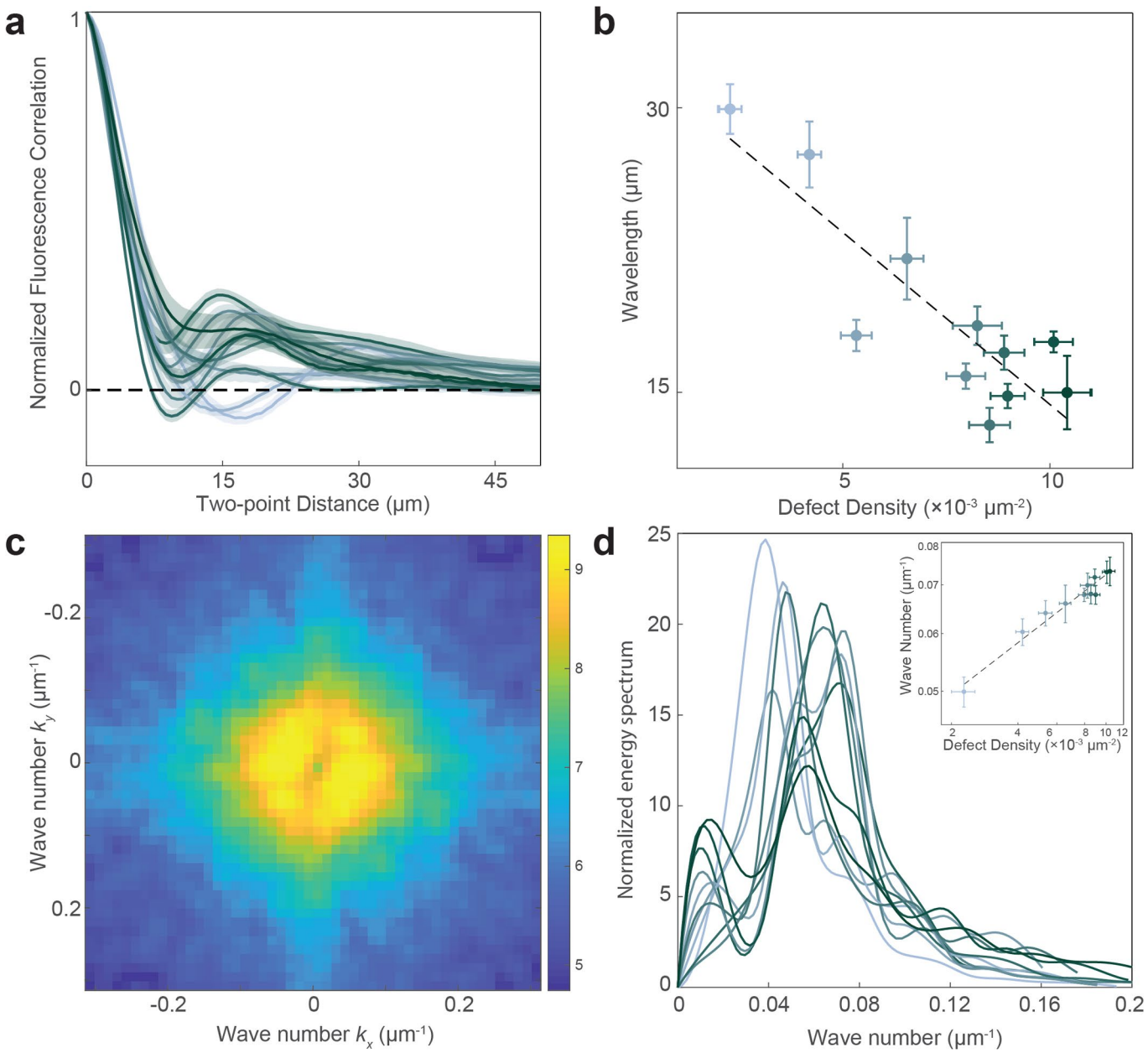

Extended Data Fig. 3 | Extracting characteristic wavelength and wave number from steady state patterns. a, Normalized intensity cross-correlation curves for 11 patterns. Shaded region: Standard error throughout time frames. **b**, Characteristic wavelength inversely correlates with defect density. Error bar: Standard deviation of quantities throughout time frames. Dashed line is the best linear fit. **c**, Example 2D energy spectrum from one pattern snapshot. Heat map color was scaled logarithmically for optimal visualization. **d**, Normalized 1D energy spectrum used to calculate the characteristic wave number shown in Fig. 1i (inset).

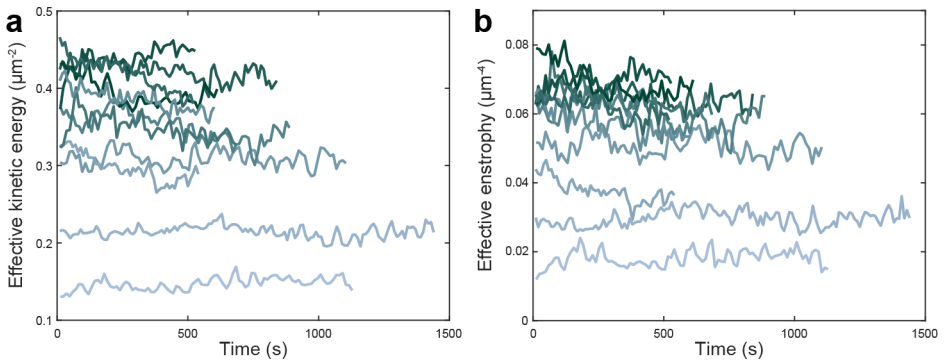

Extended Data Fig. 4 | Time series of effective kinetic energy and effective enstrophy. a, Effective kinetic energy $E(t)$ plotted as a function of time. **b**, Effective enstrophy $\Omega(t)$ plotted as a function of time.

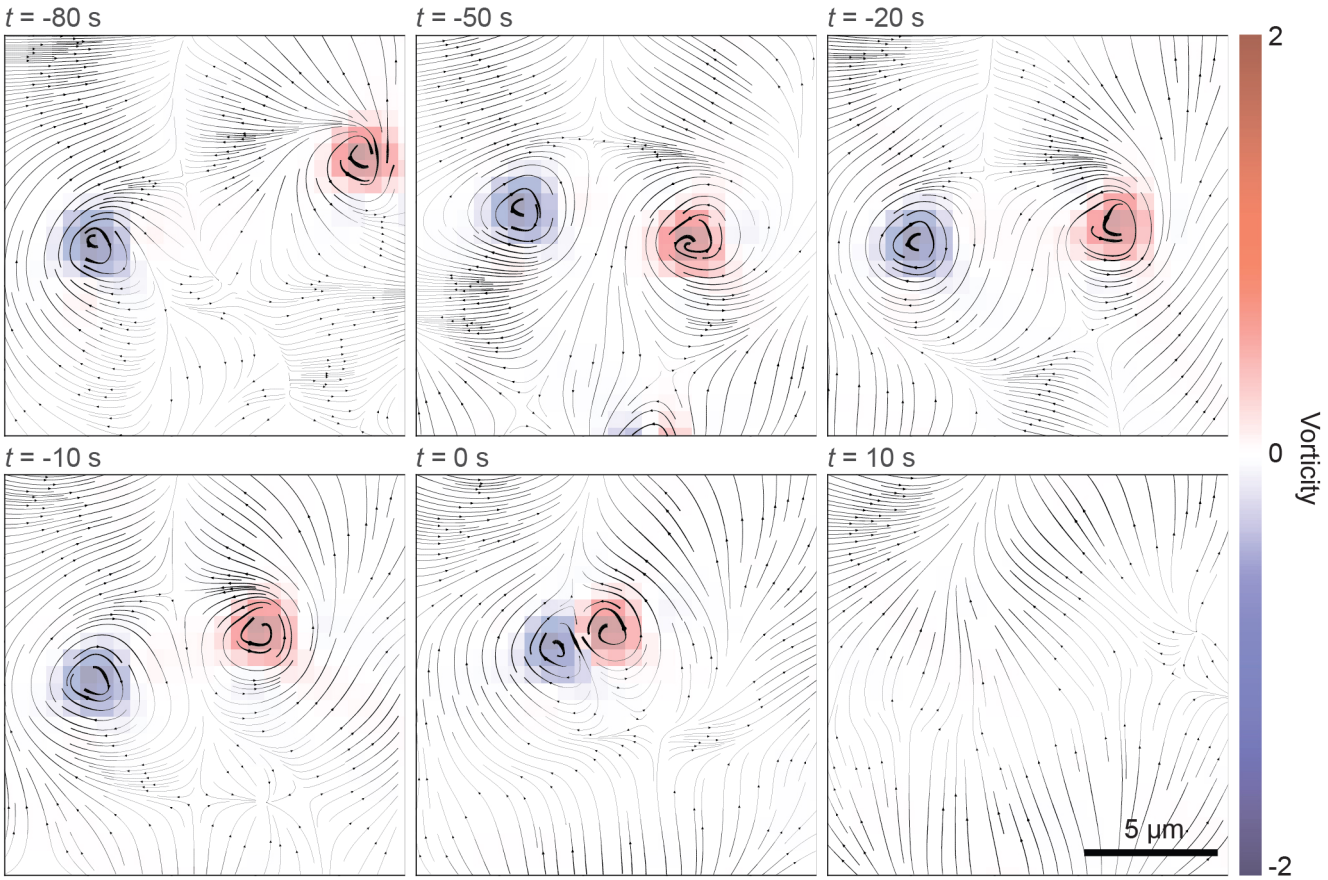

Extended Data Fig. 5 | Streamlines of phase velocity field are deformed during an annihilation event.

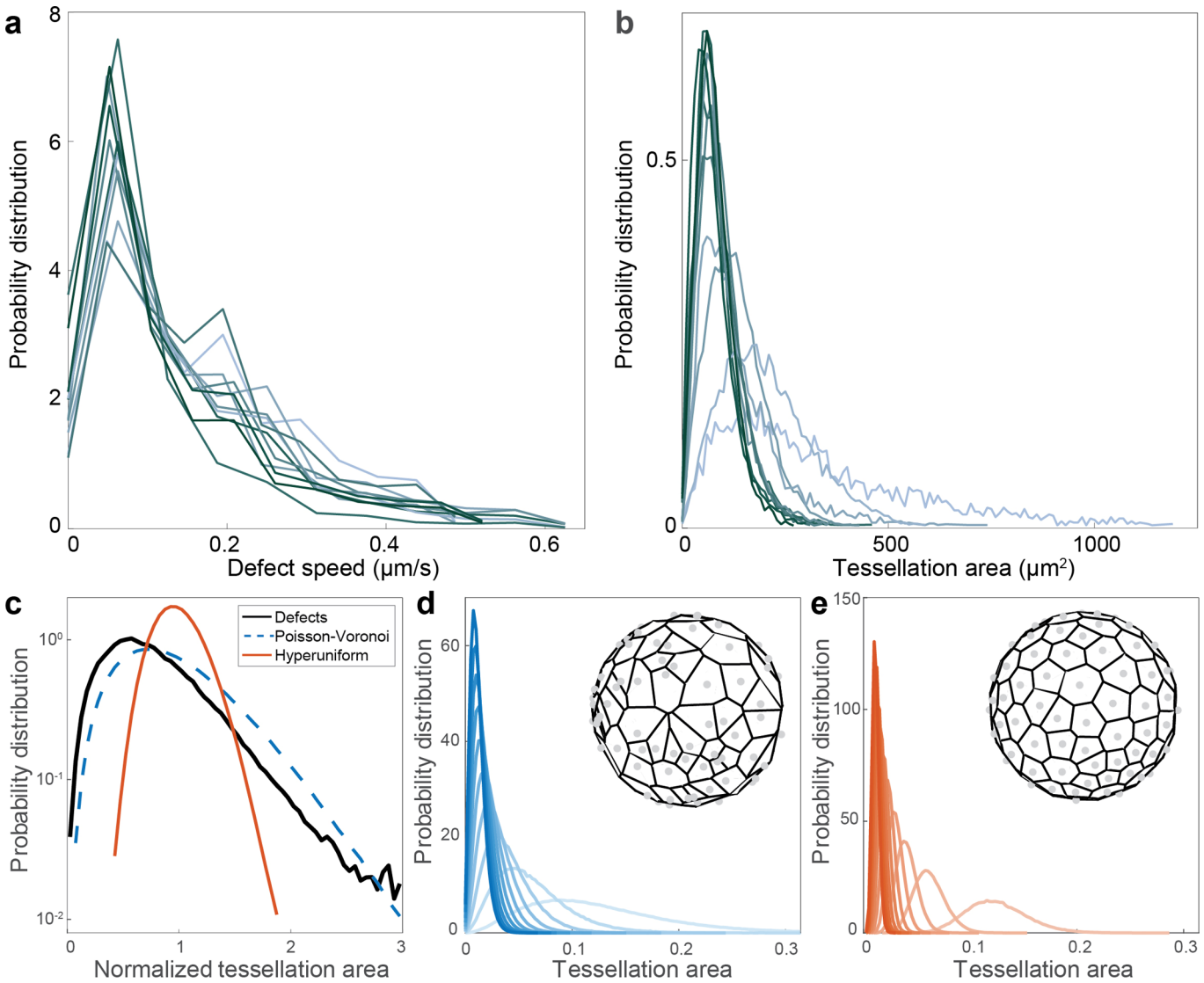

Extended Data Fig. 6 | Defect speed and Voronoi tessellation distributions. a, Defect speed statistics for 11 states, as plotted in Fig. 3a. **b**, Voronoi tessellation area statistics for 11 states, as plotted in Fig. 3b. **c**, Normalized area distribution of Poisson Voronoi cells (blue dashed), hyperuniform Voronoi cells (orange) on a sphere, and defect Voronoi cells (black, same as in Fig. 3b). **d**, and **e**, Voronoi area distribution for Poisson (**d**) and hyperuniform points (**e**) for point density $\Lambda = 100, 200, \ldots, 1000$ obtained by averaging $N = 10000$ and $N = 1000$ realizations respectively. Insets: Snapshot of a Poisson Voronoi distribution (**d**) and hyperuniform Voronoi distribution (**e**).

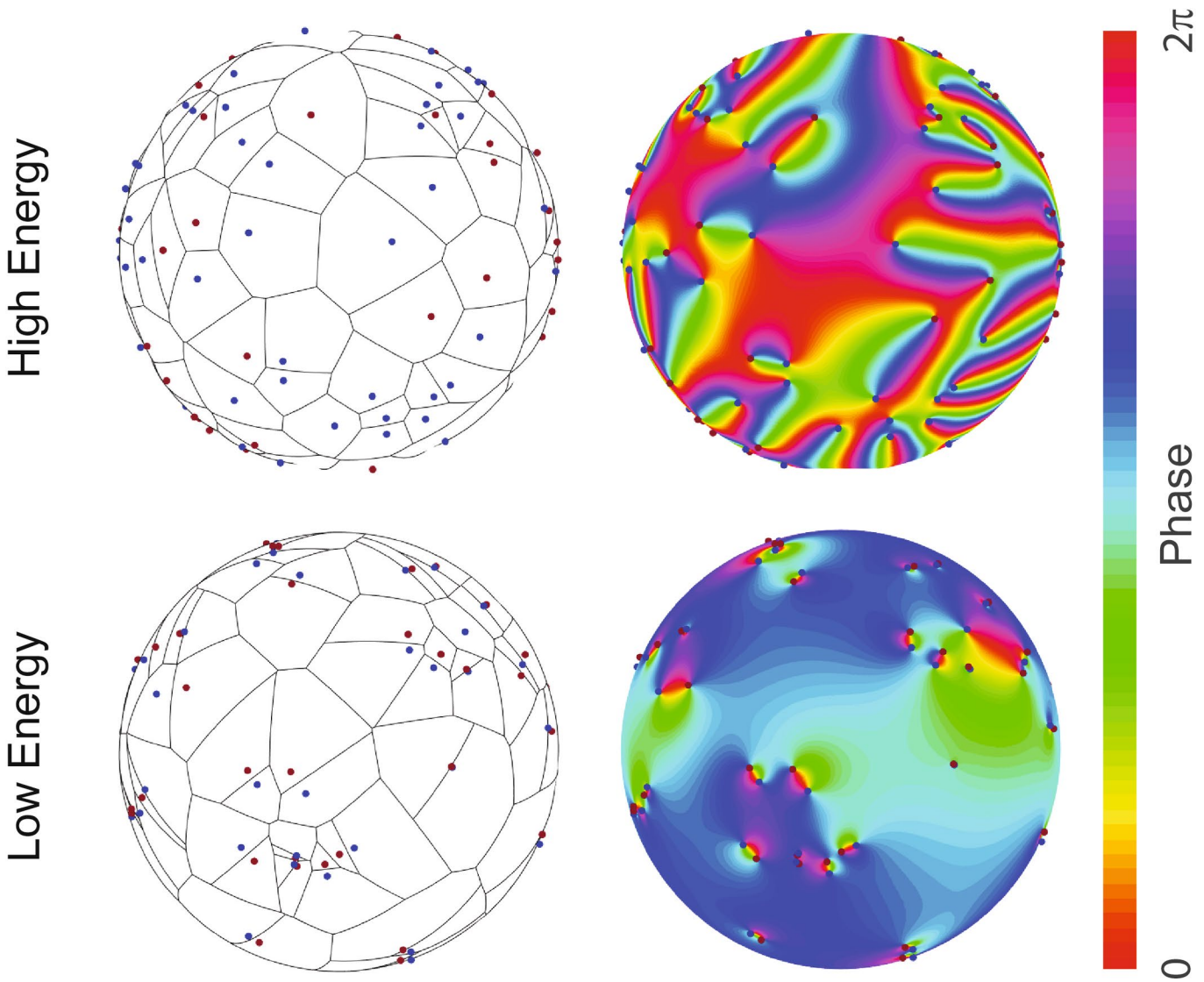

Extended Data Fig. 7 | Helmholtz-Onsager point vortex simulation at high and low energies. Example of Voronoi cells (left) and phase fields (right) for additional energy values, as in Fig. 3g, corresponding to the red (high energy) and blue (low energy) lines in Fig. 3c. In the high energy regime, like-charge vortices cluster, while opposite charge vortices form pairs in the low energy regime.

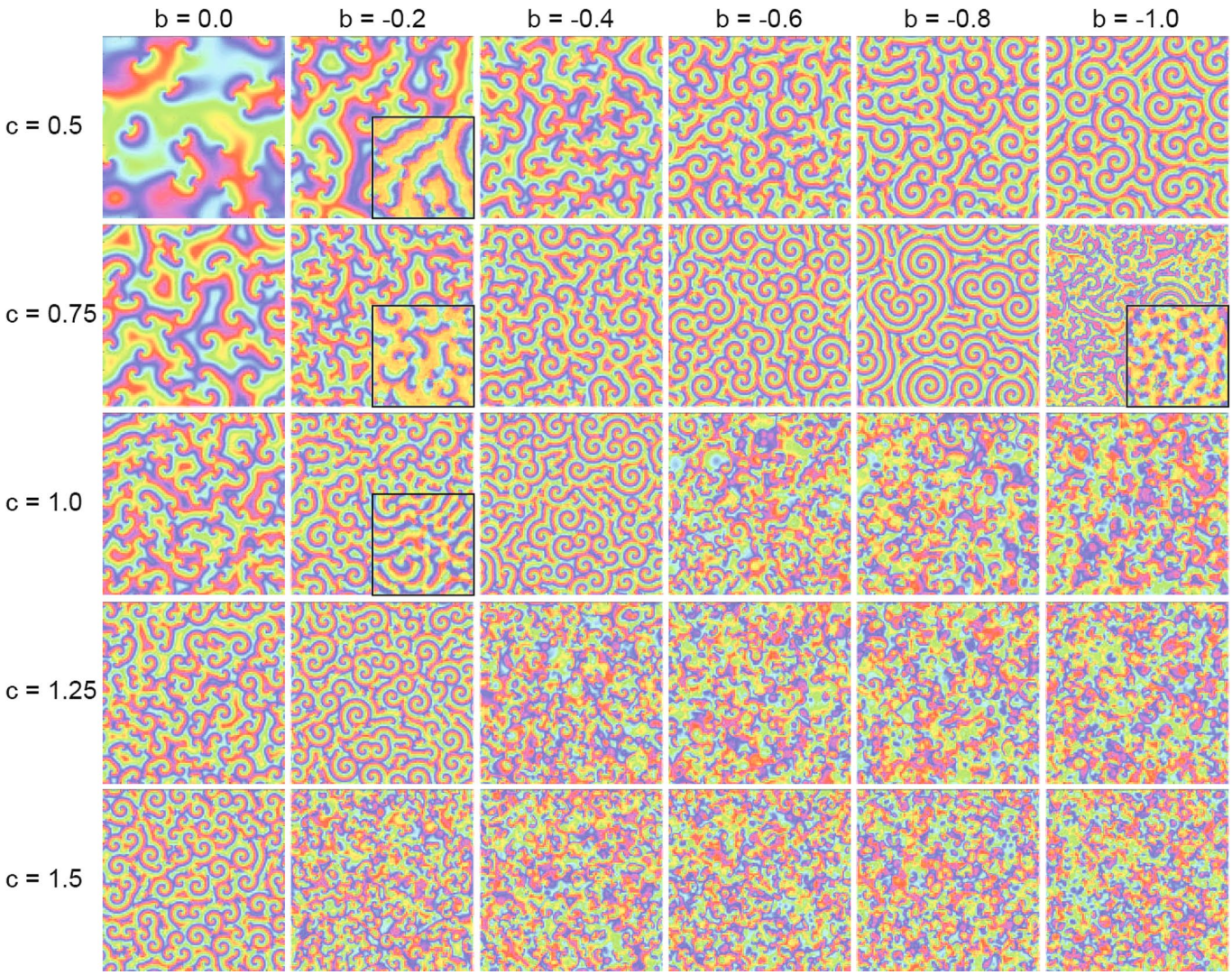

Extended Data Fig. 8 | Morphologies of spirals in CGL parameter space. Snapshots of spiral reaction diffusion waves taken at steady state for various values of *b* an *c*. Simulations here were done on a 500 ×500 grid, but in all other respects are the same as described in the Methods section. Images are from time $T = 400$. Insets correspond to experimentally observed morphologies, matched according to the procedure described in Methods.

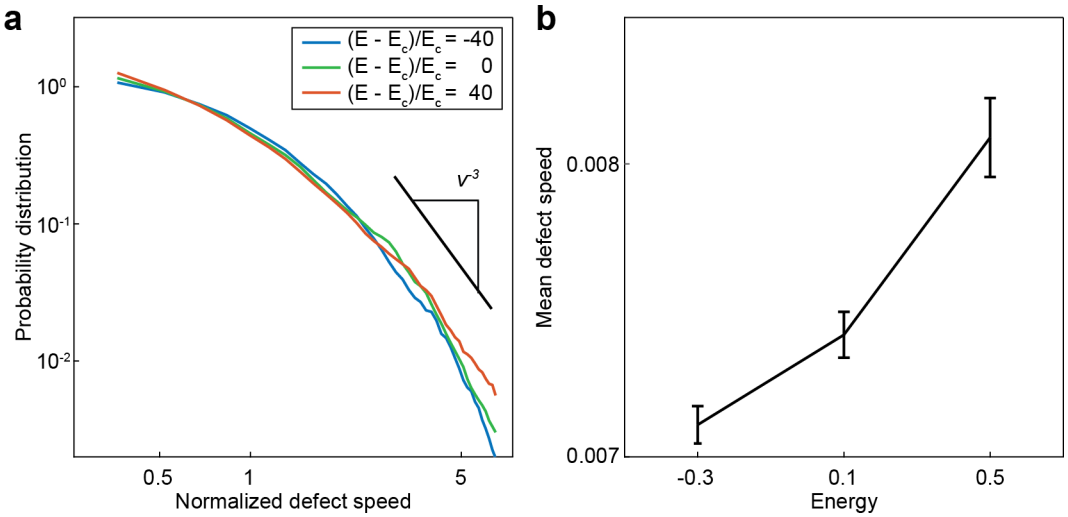

Extended Data Fig. 9 | Speed statistics for defects interacting pairwise with a Bessel-form potential. a, Probability distribution of normalized defect speed at three different energy levels (sub-critical, critical, super-critical). **b**, Mean defect scalar velocities as a function of total energy, scaled by the energy difference compared to the critical state. Error bars correspond to variance in speed for individual defects.

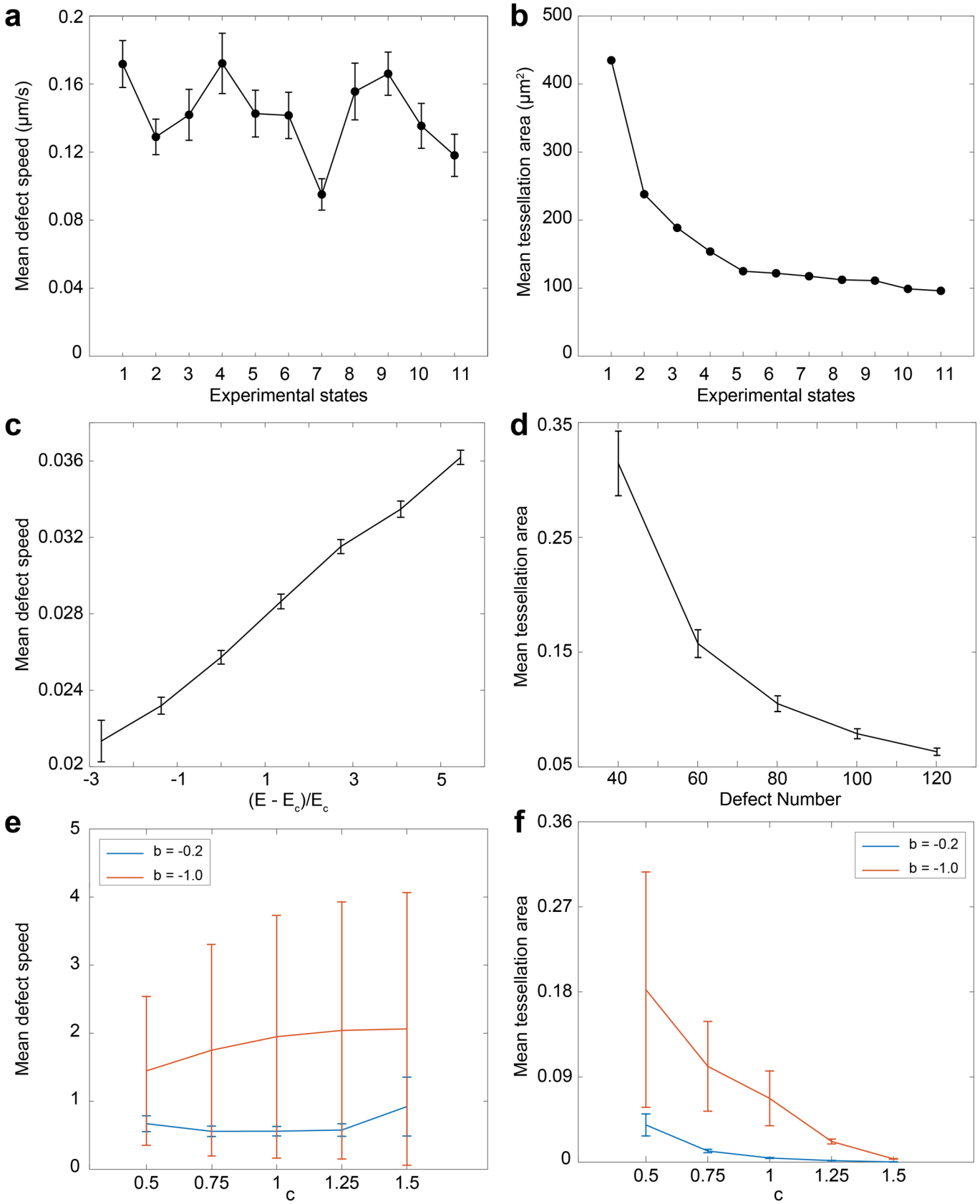

Extended Data Fig. 10 | See next page for caption.

Extended Data Fig. 10 | Mean statistics of vortex speed and area for experimental and simulated states. a, Mean vortex speeds for each experimental state used to normalize speed (Extended data Fig 6a) to obtain Fig. 3a. Error bars correspond to variance of speed distribution. **b**, Mean Voronoi tessellation areas for each experimental state used to normalize Voronoi tessellation areas (Extended data Fig 6b) to obtain Fig. 3b. **c**, Mean speed of vortices in point-vortex model as a function of deviation from critical energy. Error bars correspond to variance of speed distribution. **d**, Mean Voronoi tessellation areas used to normalize main text Fig. 3d. Error bars show variance of single particle area distribution. **e**, Mean vortex speeds for CGL simulations as a function of parameter b and c. Error bars correspond to variance in speed for individual vortices. **f**, Mean Voronoi tessellation areas for CGL simulations in Fig. 3i: Error bars correspond to variance in domain size for an individual vortex.

nature research

Corresponding author(s): Nikta Fakhri, Joern Dunkel

Last updated by author(s): Jan 7, 2020

Reporting Summary

Nature Research wishes to improve the reproducibility of the work that we publish. This form provides structure for consistency and transparency in reporting. For further information on Nature Research policies, see Authors & Referees and the Editorial Policy Checklist.

Statistics

For all statistical analyses, confirm that the following items are present in the figure legend, table legend, main text, or Methods section.

n/a	Confirmed	
☐	☒	The exact sample size (*n*) for each experimental group/condition, given as a discrete number and unit of measurement
☐	☒	A statement on whether measurements were taken from distinct samples or whether the same sample was measured repeatedly
☒	☐	The statistical test(s) used AND whether they are one- or two-sided *Only common tests should be described solely by name; describe more complex techniques in the Methods section.*
☒	☐	A description of all covariates tested
☒	☐	A description of any assumptions or corrections, such as tests of normality and adjustment for multiple comparisons
☒	☐	A full description of the statistical parameters including central tendency (e.g. means) or other basic estimates (e.g. regression coefficient) AND variation (e.g. standard deviation) or associated estimates of uncertainty (e.g. confidence intervals)
☒	☐	For null hypothesis testing, the test statistic (e.g. *F*, *t*, *r*) with confidence intervals, effect sizes, degrees of freedom and *P* value noted *Give P values as exact values whenever suitable.*
☒	☐	For Bayesian analysis, information on the choice of priors and Markov chain Monte Carlo settings
☒	☐	For hierarchical and complex designs, identification of the appropriate level for tests and full reporting of outcomes
☒	☐	Estimates of effect sizes (e.g. Cohen's *d*, Pearson's *r*), indicating how they were calculated

Our web collection on statistics for biologists contains articles on many of the points above.

Software and code

Policy information about availability of computer code

Data collection	Zeiss confocal LSM 700 used to collect data is operated using Zen software.
Data analysis	Software for determining phase field and phase singularity, and for simulation of the point vortex model, is developed in the lab and are available upon request. Particle tracking is done using software developed by Jean-Yves Tinevez. The code is deposited on Matlab FileExchange https://www.mathworks.com/matlabcentral/fileexchange/34040-simple-tracker.

For manuscripts utilizing custom algorithms or software that are central to the research but not yet described in published literature, software must be made available to editors/reviewers. We strongly encourage code deposition in a community repository (e.g. GitHub). See the Nature Research guidelines for submitting code & software for further information.

Data

Policy information about availability of data

All manuscripts must include a data availability statement. This statement should provide the following information, where applicable:

- Accession codes, unique identifiers, or web links for publicly available datasets
- A list of figures that have associated raw data
- A description of any restrictions on data availability

Data is available upon request.

Field-specific reporting

Please select the one below that is the best fit for your research. If you are not sure, read the appropriate sections before making your selection.

☒ Life sciences ☐ Behavioural & social sciences ☐ Ecological, evolutionary & environmental sciences

For a reference copy of the document with all sections, see nature.com/documents/nr-reporting-summary-flat.pdf

Life sciences study design

All studies must disclose on these points even when the disclosure is negative.

Sample size	The number of particle trajectories within each oocytes ranges from 50-200 and dynamics are observed for at least 750s.
Data exclusions	Defects which do not form trajectories (i.e. only appear for 1 frame) are considered spurious detection and are omitted from data analysis.
Replication	11 replicates are shown in the paper.
Randomization	Not relevant to study.
Blinding	Not relevant to study.

Reporting for specific materials, systems and methods

We require information from authors about some types of materials, experimental systems and methods used in many studies. Here, indicate whether each material, system or method listed is relevant to your study. If you are not sure if a list item applies to your research, read the appropriate section before selecting a response.

Materials & experimental systems

n/a	Involved in the study
☒	☐ Antibodies
☒	☐ Eukaryotic cell lines
☒	☐ Palaeontology
☐	☒ Animals and other organisms
☒	☐ Human research participants
☒	☐ Clinical data

Methods

n/a	Involved in the study
☒	☐ ChIP-seq
☒	☐ Flow cytometry
☒	☐ MRI-based neuroimaging

Animals and other organisms

Policy information about studies involving animals; ARRIVE guidelines recommended for reporting animal research

Laboratory animals	Patiria Miniata
Wild animals	Wild starfish Patiria Miniata was procured from South Coast Bio-Marine LLC. The animals were kept in salt water fish tank maintained at 15 °C. Due to their wound healing capacity, multiple rounds of oocytes harvesting can be done without sacrificing the starfish.
Field-collected samples	Not relevant for study.
Ethics oversight	No ethical requirement since the animal is invertebrate.

Note that full information on the approval of the study protocol must also be provided in the manuscript.